Three-dimensional imaging of flat natural and cultural heritage objects by a Compton scatter modality

Patricio Guerrero Prado[a,b,c], Mai K. Nguyen[b], Laurent Dumas[c], and Serge X. Cohen[a,*]

[a]IPANEMA , CNRS USR 3461/MCC/UVSQ, BP48 Saint-Aubin, 91192 Gif-sur-Yvette, France
[b]Equipes Traitement de l'Information et Systèmes, ENSEA/Cergy-Pontoise University/CNRS UMR 8051, 2 rue Adolphe Chauvin, 95302 Cergy-Pontoise, France
[c]Laboratoire de Mathématiques de Versailles, CNRS UMR 8100/Versailles University, 45 avenue des Etats-Unis, 78035 Versailles, France

December 2016

Abstract

Characterisation and interpretation of flat ancient material objects, such as those found in archaeology, palaeoenvironments, palaeontology and cultural heritage, have remained a challenging task to perform by means of conventional X-ray tomography methods due to their anisotropic morphology and flattened geometry. To overcome limitations of mentioned methodologies for such samples, a new imaging modality based on Compton scattering is proposed in this work. Classical X-ray tomography treats Compton scatter data as noise in the image formation process, while in Compton scatter tomography the conditions are set such that Compton data becomes the principal image contrasting agent. Under this conditions, we are able, on the first hand, to avoid relative rotations between the sample and the imaging setup, and on the other hand, to obtain three dimensional data even when the object is supported by a dense material by exploiting back-scattered photons. Mathematically this problem is addressed by means of a Conical Radon transform and its inversion. Image formation process and object reconstruction model are presented. Feasibility of this methodology is supported by numerical simulations.
Keywords: Radon transform, Compton scatter tomography, Ancient material objects, Image reconstruction

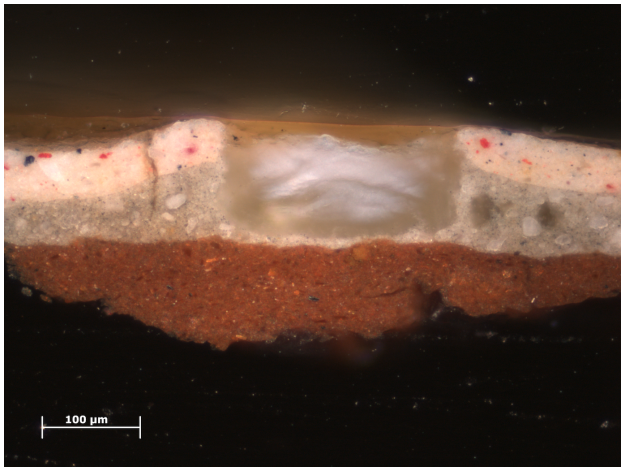

Figure 1: Paint cross-section showing a stratigraphical assemblage of *The Anatomy Lesson of Dr. Nicolaes Tulp*, 1632 by Rembrandt, Mauritshuis, The Hague. © Sample taken and prepared as cross-section by P. Noble during the conservation treatment of the painting in 1997, and re-photographed by A. van Loon, Mauritshuis, in 2010 for the Rembrandt Database.

1 Introduction

1.1 Context

Material characterisation of ancient flat objects encountered in natural or cultural heritage remains notably challenging with nowadays X-ray imaging methods. When one deals with heritage objects, the non-invasiveness and non-destructiveness properties of inspections are a requirement that X-ray imaging methodologies provides, enabling two-dimensional imaging of the sample. However, one can easily be facing samples presenting a flattened geometry, that is, samples presenting a large ratio between its front area and thickness. The challenge is then to perform a three-dimensional probing without using a relative rotation between the sample and the imaging setup as would be done in conventional tomography, using either absorption or phase contrast modality, since probing would suffer from the high differential light path in distinct directions.

Samples presenting such characteristics are encountered in, for example, studies of conservation/restoration of easel painting requiring the characterisation of the stratigraphical assemblage of pigments often over a very dense background layer such as one made of white lead. An example of this kind of studies is shown in Fig. 1 which was performed by means of an invasive method. Fig. 2 presents another example of objects possessing this morphology, namely in palaeontology with the Lagerstätten fossils [2] which are mechanically flat-

Figure 2: A flat fossil actinopterygian over a high thick X-ray absorbing support from the Kem Kem Beds in Morocco dated back to the Lower Cretaceous (95 million years ago). © P. Gueriau (MHNM/MNHN).

tened during the fossilisation process and stand on one side of a thick sedimental slab which can not be thinned for the study. In both cases the volume of interest forms a layer on top of a material support which is opaque to X-ray either due to its density or its thickness.

Two alternatives are available to work out this issue : either to perform a stratigraphical section of the sample which is an invasive method, or to limit the study to a bi-dimensional analysis limited to the front surface of the sample, for example with synchrotron X-ray fluorescence spectral raster-scanning as performed in Ref. [2], remaining however a three-dimensional study still uncovered. Furthermore, because of the opaque supporting material, transmission and forward scattering data, that is, with a scattering angle inferior of $\frac{\pi}{2}$, is impossible to collect. This motivates the proposal of a modality tapping on back-scattered data, that is, data collected with a scattering angle ω comprised between $\frac{\pi}{2}$ and π, as shown in Fig. 3. In the following, we will call $\bar{\omega} = \pi - \omega$ the supplementary angle of ω.

Identity (1) introduces the Compton Equation, a diffeomorphism between the scattering angle and the scattered energy under the hypotheses that electrons are both free and at rest and that the incident beam is monochromatic, that is, a single value E_0 of an incident energy is radiating the object. Equation (1) provides a reliable approximation of a real scattering scenario and by means of it, the scattering image formation process corresponds to a Radon transform over the surface of a cone with fixed axis direction [6, 3, 1] .

1.2 Compton scatter tomography (CST)

Laying on the energy range from 50 eV up to 1 GeV, the dominant photon-matter interaction processes are the photoelectric absorption, electron-positron pair production, Rayleigh scattering which is both elastic and coherent, and Compton scattering which conversely is both inelastic and incoherent. In this last one, an incident photon of energy E_0 is absorbed by a target electron, who re-emits a secondary photon scattered by an angle ω relative to the direction

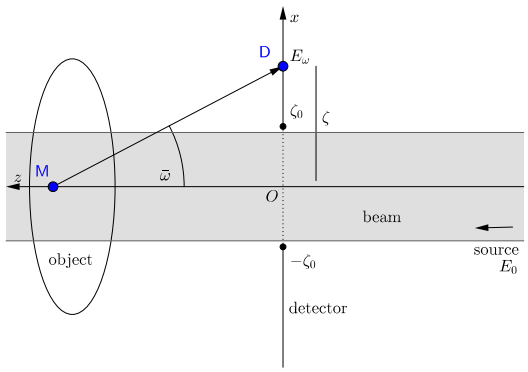

Figure 3: Compton back-scattering fundamentals. A photon of energy E_0 is Compton scattered by an angle $\omega = \pi - \bar{\omega}$ generating a new photon of energy E_ω.

of the original photon. The scattered photon has then an energy E_ω which is related to the scattering angle ω by (1), the Compton equation, presented later.

In classical X-ray imaging and tomography, Compton scattered signal is considered as noise added to photoelectric absorption and coherent scattered data. This is because X-ray transmission signal is dominated by the photoelectric absorption whilst coherent scattering may produce significant amplitude variations at low scattering angles thanks to constructive and destructive interference effects due to the coherent nature of this scattering. However, depending on the material, if the incident radiation has an energy superior of about 4×10^4 electron-volts, Compton scattering becomes the dominant phenomenon in the process, even more when detection is performed outside the direct transmission area ($\omega = 0$).

Classical tomographic imaging modalities, developed and used in most all applications in the last half century include : Transmission Computed Tomography, Single Photon Emission Tomography and Positron Emission Tomography. All of them regard primary radiation and perform 3D mappings leaning on relative rotations between the object and the imaging setup. In such framework, Compton scattering events are adding a non-uniform background to the observation, a systematic bias which leads to artefacts in the reconstruction if it is not accounted for. As the relative importance of the Compton scattering effect over the other two processes mentioned above is increasing with an increase on incident energy, its effect is even more important when using higher energy γ-ray imaging.

The idea of exploiting scattered radiation by Compton effect in imaging techniques has been introduced and studied simultaneously and it has given birth to CST [7, 6, 5, 1, 8, 9], which focuses to reconstruct the electron density

map of the object.

To compensate the information provided by multiple projections angles in classical tomography, CST exploits the energy loss of the scattered photons. This energy loss is related to he scattering angle via the Compton equation given by

$$E_\omega = \frac{E_0}{1 + \dfrac{E_0}{m_e c^2}(1 - \cos\omega)}, \tag{1}$$

where $m_e c^2 = 511$ keV is the rest mass energy of the electron.

The first CST scanner was proposed in 1994 [7] through a Radon transform over arc of circles starting at a γ-ray source and ending at a fixed detecting site. Radon transforms over conical surfaces having fixed axis directions and variable opening angle are studied in Ref. [6] where a first analytic inversion formula is proposed using circular component analysis, with applications to emission imaging based on Compton scattered radiation. Generalisations of this kind of transforms to higher dimensions spaces with related inverse formulae in a filtered backprojection type are presented in Ref. [3]. A backprojection inversion algorithm for a conical Radon transform in $\mathbb{R}^3$ was developed recently in Ref. [1].

This paper is organised as follows. Section 2 describes the imaging configuration. Section 3 defines the Conical Radon Transform and presents image formation process. Section 4 details object reconstructions via a backprojection inversion from Ref.[1]. In Section 5 we present numerical scheme and simulation results for flat objects both for energy resolved image formation and sample reconstruction. Finally, Section 6 closes this work with conclusions and perspectives.

2 Proposed setup

CST aims to reconstruct the *electron density* map of the studied object. In this work, the electron density is represented mathematically by a nonnegative bump function (both smooth and of bounded support) $f : \mathbb{R}^2 \times \mathbb{R}^+ \to \mathbb{R}^+$.

Essentially, as shown in Fig. 4, an incident photon of energy E_0, belonging to a monochromatic parallel beam with a square section, is Compton scattered by an electron situated inside the object at M subtending an angle ω ($\frac{\pi}{2} < \omega < \pi$) with the direction of incidence. The scattered photon, of energy E_ω approximated by (1), reaches a detecting site $\mathsf{D} = (\zeta, \xi, 0)$ on the 2D detector that is located over the xOy-plane. The parallel beam is centred at the Oz-axis.

The imaging configuration is described then as follows : As mentioned, a synchrotron radiation setup with a parallel monochromatic X-ray beam (about 50 keV) and a space-energy resolved detector are considered. As represented in Fig. 4, the detector will be placed between the source and the object to capture back-scattered photons. It will have a hole in the middle of area $4\zeta_0\xi_0$ for some two positive real numbers (ζ_0, ξ_0) to allow the beam to go through. Therefore, we will have data for values of (ζ, ξ) on the xOy-plane verifying $|\zeta| > \zeta_0$ and

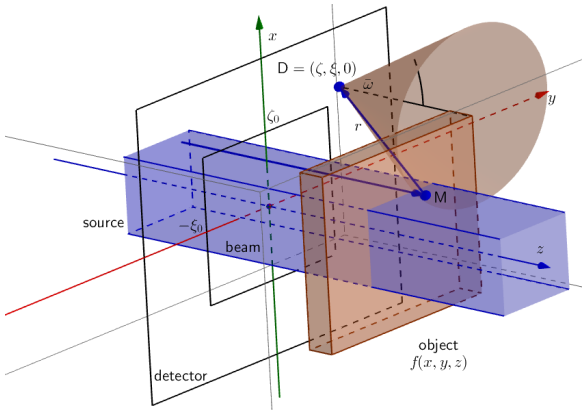

Figure 4: Imaging configuration proposed. A scattering site M produces scattered radiation captured at a detecting site D. The incident photon is coming from a parallel beam with a square cross-section.

$|\xi| > \xi_0$. Horizontal and vertical translations of the sample will be needed to allow the imaging of the full object.

3 Image formation

3.1 The Conical Radon transform (CRT)

The Conical Radon Transform[6, 3] integrates a function over circular cone surfaces, its backprojection reconstruction procedure is developed in Ref. [1].

A (ψ, r)-parametrisation of the lateral surface of a circular cone is considered, where φ is the azimuthal angle and r the distance of a point in the cone surface from its vertex. Such parametrisation reads, for a cone with vertex at $\mathsf{D} = (\zeta, \xi, 0)$ and opening angle ω, noted $\mathcal{C}_{\omega,\mathsf{D}}$,

$$\mathcal{C}_{\omega,\mathsf{D}} = (\zeta + r\sin\omega\cos\psi, \xi + r\sin\omega\sin\psi, r\cos\omega). \tag{2}$$

Therefore, the CRT applied on a electron density function f, noted Cf, defined as the integral of this function over the surface of a cone parametrised as (2) reads

$$Cf(\zeta,\xi,\omega) = \int_0^\infty \int_0^{2\pi} \frac{1}{r} f(\zeta + r\sin\omega\cos\psi, \xi + r\sin\omega\sin\psi, r\cos\omega)\,\mathrm{d}\psi\,\mathrm{d}r. \tag{3}$$

The factor $\dfrac{1}{r}$ comes from the integration measure on the cone $r\sin\omega\,\mathrm{d}\psi\,\mathrm{d}r$ and the approximation of the solid angle $\dfrac{1}{r^2}\cos\omega$, the factor $\sin\omega\cos\omega$ not

appearing in last integral will be taken into account later in the scattered photon flux time density in (9).

It may be useful to express (3) as an integral with respect to $z = r\cos\omega$ and introducing the variable $t = \tan\omega$. If notation Cf is conserved, (3) is also expressed as

$$Cf(\zeta,\xi,t) = \int_0^{\infty}\int_0^{2\pi} \frac{1}{z} f(\zeta + tz\cos\psi, \xi + tz\sin\psi, z)\,\mathrm{d}\psi\,\mathrm{d}z. \tag{4}$$

3.2 Scattered photon flux time density

Let $I(E_\omega, \mathsf{D})$ represent the recorded scattered photon flux density (number of photons of energy E_ω recorded per unit time at D). It incorporates the following parameters :

- I_0: the incident photon flux time density just before the scattering event at M.
- $\sigma(\omega)$: the Klein-Nishina differential cross-section [4] at an angle ω.
- $f(\mathsf{M})$: the electron density at M.
- $\mathrm{d}\Omega(\mathsf{M},\mathsf{D})$: the solid angle from M to D.
- $\mathrm{d}\mathsf{M}$: the area element around M over the cone surface.

The solid angle $\mathrm{d}\Omega(\mathsf{M},\mathsf{D})$ can be seen from Fig. 4 to be

$$\mathrm{d}\Omega(\mathsf{M},\mathsf{D}) = 4\arctan\big(\frac{1}{4r^2}\tau\cos\bar{\omega}\big), \tag{5}$$

where τ is the area of the detecting element located at D and r the Euclidean distance from M to D.

If τ is small enough, then $\mathrm{d}\Omega(\mathsf{M},\mathsf{D})$ can be approximated by $\dfrac{1}{r^2}\tau\cos\bar{\omega}$.

The Klein-Nishina differential cross-section is a function of the scattering angle ω giving the probability of a photon to be scattered in a given direction ω when the azimuthal angle is uniformly distributed in the interval $(0, 2\pi)$. It is given by[4]

$$\sigma(\omega) = \frac{1}{2}r_e^2\left(\frac{E_\omega}{E_0}\right)^2\left(\frac{E_\omega}{E_0} + \frac{E_0}{E_\omega} - \sin^2\omega\right), \tag{6}$$

where r_e is the classical electron radius. The factor $\frac{1}{2}r_e^2$ comes from the diametrical transversal area of an electron πr_e^2 and the uniformity of the azimuthal angle $\frac{1}{2\pi}$.

Consequently, the scattered photon flux density at D, given a scattering site M reads

$$\mathrm{d}I(E_\omega, \mathsf{D}|\mathsf{M}) = I_0\,\sigma(\omega)\,\mathrm{d}\Omega(\mathsf{M},\mathsf{D})\,f(\mathsf{M})\,\mathrm{d}\mathsf{M} \tag{7}$$

The total scattered flux time density $I(E_\omega, \mathsf{D})$ recorded at D is the integral over all scattering sites laying over the surface of the cone $\mathcal{C}_{\bar{\omega},\mathsf{D}}$. It is hence given by the integral

$$I(E_\omega, \mathsf{D}) = \int\limits_{\mathsf{M}\in\mathcal{C}_{\bar{\omega},\mathsf{D}}} \mathrm{d}I(E_\omega, \mathsf{D}|\mathsf{M}). \tag{8}$$

From the last integral, we can extract the Conical Radon transform, and we are able to express the scattered photon flux density for a recorded energy E as

$$I(E, \mathsf{D}) = \tau I_0 \sin\bar{\omega}_E \cos\bar{\omega}_E \ \sigma(\omega_E) Cf(\bar{\omega}_E, \zeta, \xi). \tag{9}$$

Note the use of ω_E and $\bar{\omega}_E$, the scattering angle and its supplementary, related to the recorded energy E approximated by an inversion of identity (1).

4 Object reconstruction

4.1 Bessel function and Hankel transform

We recall the Bessel function of the first kind of order 0, and the Hankel transform of a function f of order 0 noted respectively J_0 and h_0,

$$J_0(x) = \frac{1}{2\pi} \int\limits_0^{2\pi} e^{ix\sin\alpha}\,\mathrm{d}\alpha, \tag{10}$$

$$h_0 f(k) = \int\limits_0^{\infty} f(r) J_0(kr) r\,\mathrm{d}r. \tag{11}$$

The inverse expression of the Hankel transform reads

$$f(r) = \int\limits_0^{\infty} h_0 f(k) J_0(kr) k\,\mathrm{d}k. \tag{12}$$

4.2 Inverse formula

We start writing the bidimensional (ζ, ξ)-Fourier transform of (4) as

$$\widehat{Cf}(u,v,t) = \int\limits_0^{\infty}\int\limits_0^{2\pi}\int\limits_{\mathbb{R}^2} \frac{1}{z} f(\zeta + tz\cos\psi, \xi + tz\sin\psi, z) e^{-2\pi i(u\zeta+v\xi)}\,\mathrm{d}\zeta\mathrm{d}\xi\,\mathrm{d}\psi\mathrm{d}z, \tag{13}$$

and with a change of variables (translation of the vertex to the origin) $x = \zeta + tz\cos\psi$ and $y = \xi + tz\sin\psi$, (13) becomes

$$\begin{aligned}\widehat{Cf}(u,v,t) = \int\limits_0^{\infty}\int\limits_0^{2\pi} \frac{1}{z} \int\limits_{\mathbb{R}^2} f(x,y,z) e^{-2\pi i(ux+vy)}\,\mathrm{d}x\mathrm{d}y \\ e^{2\pi i t z(u\cos\psi + v\sin\psi)}\,\mathrm{d}\psi\mathrm{d}z,\end{aligned} \tag{14}$$

where we recognize the (x, y)-Fourier transform of f and then last expression reads

$$\widehat{Cf}(u, v, t) = \int_0^\infty \frac{1}{z} \hat{f}(u, v, z) \int_0^{2\pi} e^{2\pi i t z (u \cos\psi + v \sin\psi)} \, \mathrm{d}\psi \mathrm{d}z, \tag{15}$$

where we can identify the Bessel function of the first kind of order 0 by switching to polar coordinates *via* $u = q\cos\beta$ and $v = q\sin\beta$ by

$$\begin{aligned} \widehat{Cf_p}(q, \beta, t) &= \int_0^\infty \frac{1}{z} \hat{f}_p(q, \beta, z) \int_0^{2\pi} e^{2\pi i q t z \cos(\beta - \psi)} \, \mathrm{d}\psi \mathrm{d}z \\ &= 2\pi \int_0^\infty \frac{1}{z} \hat{f}_p(q, \beta, z) J_0(2\pi q t z) \, \mathrm{d}z. \end{aligned} \tag{16}$$

Note the use of notation $\widehat{Cf_p}$ and $\hat{f}_p$ to point out the use of polar coordinates.

Last integral turns out to be the Hankel transform of the function $g : z \to \frac{1}{z^2} \hat{f}_p(q, \beta, z)$, then (16) reads

$$\widehat{Cf_p}(q, \beta, t) = 2\pi h_0 g(2\pi q t). \tag{17}$$

One can therefore apply the Hankel inverse formula to have

$$g(z) = \frac{1}{2\pi} \int_0^\infty \widehat{Cf_p}(q, \beta, t) J_0(2\pi q z t) 2\pi q t \, \mathrm{d}(2\pi q t). \tag{18}$$

Then, going back to $\hat{f}_p$ from g, we have

$$\hat{f}_p(q, \beta, z) = 2\pi z^2 q^2 \int_0^\infty \widehat{Cf_p}(q, \beta, t) J_0(2\pi q z t) \, \mathrm{d}t. \tag{19}$$

And finally, take the inverse Fourier transform in polar coordinates to recover f as

$$f(x, y, z) = 2\pi z^2 \int_0^{2\pi} \int_0^\infty \int_0^\infty \widehat{Cf_p}(q, \beta, t) J_0(2\pi q t z) t \, \mathrm{d}t \, q^3 e^{2\pi i q (x\cos\beta + y \sin\beta)} \, \mathrm{d}q \mathrm{d}\beta. \tag{20}$$

Last integral may be expressed in Cartesian coordinates related to the Fourier domain (u, v) and in terms of ω, and then we are able to write the inverse

formula of (3) as

$$f(x,y,z) = 2\pi z^2 \int_{\mathbb{R}^2} (u^2+v^2) e^{2\pi i(ux+vy)} \int_0^{\pi/2} \frac{\sin\omega}{\cos^3\omega} \widehat{Cf}(u,v,\omega) J_0(2\pi z \tan\omega\sqrt{u^2+v^2})\,\mathrm{d}\omega\,\mathrm{d}u\mathrm{d}v. \tag{21}$$

4.3 The adjoint transform

Let us introduce some basic notations. C is defined as an operator from $X := L_2(\mathbb{R}^2 \times \mathbb{R}^+)$ to $Y := L_2(\mathbb{R}^2 \times [0, \frac{\pi}{2}])$, and the respective inner products of those spaces are defined by

$$\begin{aligned} (f_1, f_2)_X &= \int_{\mathbb{R}} \int_{\mathbb{R}^2} f_1(x,y,z) f_2(x,y,z)\,\mathrm{d}x\mathrm{d}y\mathrm{d}z, \\ (g_1, g_2)_Y &= \int_{\mathbb{R}^2} \int_0^{\pi/2} g_1(\zeta,\xi,\omega) g_2(\zeta,\xi,\omega)\,\mathrm{d}\omega\mathrm{d}\zeta\mathrm{d}\xi. \end{aligned} \tag{22}$$

The adjoint transform $C^\dagger$ of C, closely related to the backprojection operator, is defined as the transform from Y to X that verifies

$$(g, Cf)_Y = (C^\dagger g, f)_X. \tag{23}$$

In order to derive an expression for $C^\dagger$, we start from the left side of last identity and introduce the definition of C given in (3) writing

$$\begin{aligned} (g, Cf)_Y &= \int_{\mathbb{R}^2} \int_0^{\pi/2} g(\zeta,\xi,\omega) Cf(\zeta,\xi,\omega)\,\mathrm{d}\omega\mathrm{d}\zeta\mathrm{d}\xi \\ &= \int_{\mathbb{R}^2} \int_0^{\pi/2} g(\zeta,\xi,\omega) \\ &\quad \int_0^{\infty} \int_0^{2\pi} \frac{1}{r} f(\zeta + r\sin\omega\cos\psi, \xi + r\sin\omega\sin\psi, r\cos\omega)\,\mathrm{d}\psi\mathrm{d}r\,\mathrm{d}\omega\mathrm{d}\zeta\mathrm{d}\xi, \end{aligned} \tag{24}$$

and apply a change of variables in the form $x = \zeta + tz\cos\psi$, $y = \xi + tz\sin\psi$

and Fubini's theorem to have

$$(g, Cf)_Y = \int_{\mathbb{R}} \int_{\mathbb{R}^2} \frac{1}{z} f(x,y,z) \int_0^{\pi/2} \int_0^{2\pi} g(x - z\tan\omega\cos\psi, y - z\tan\omega\sin\psi, \omega)\, \mathrm{d}\psi \mathrm{d}\omega\, \mathrm{d}x\mathrm{d}y\mathrm{d}z. \tag{25}$$

From where one is able to extract the adjoint transform $C^\dagger$ of C from identity (23) in the form

$$C^\dagger g(x,y,z) = \frac{1}{z} \int_0^{\pi/2} \int_0^{2\pi} g(x - z\tan\omega\cos\psi, y - z\tan\omega\sin\psi, \omega)\, \mathrm{d}\psi \mathrm{d}\omega. \tag{26}$$

The way it is defined, the adjoint transform can be interpreted here as a backprojection procedure of projections $g(x - z\tan\omega\cos\psi, y - z\tan\omega\sin\psi, \omega)$ to the position (x, y, z) times the factor $\frac{1}{z}$, *i.e.*, one assigns to (x, y, z) the values of projections started at this point, forming a cone towards the detector with opening angle ω times the mentioned factor.

For a first rough reconstruction, $f(x, y, z)$ can be approximated through the adjoint transform or equivalently in this case, through a simple backprojection of data as

$$f(x,y,z) \approx C^\dagger C f(x,y,z). \tag{27}$$

4.4 From the adjoint transform to filtered backprojections

To show that the adjoint transform $C^\dagger$ is not the inverse operator of C, one only needs to compute $C^\dagger C f(x, y, z)$ and compare the result with inversion formula of C (21) given in section 4.2. Then, filters must be added to projections in order to adjust the result of $C^\dagger C f(x, y, z)$ in accordance to such inverse formula.

Therefore, to compute $C^\dagger C f(x, y, z)$, from (23), we insert the bidimensional (ζ, ξ)-Fourier transform of C to have

$$C^\dagger C f(x,y,z) = \frac{1}{z} \int_0^{\pi/2} \int_{\mathbb{R}^2} \widehat{Cf}(u,v,\omega) e^{2\pi i(ux+vy)} \int_0^{2\pi} e^{-2\pi i z \tan\omega(u\cos\psi + v\sin\psi)}\, \mathrm{d}\psi\, \mathrm{d}u\mathrm{d}v\mathrm{d}\omega. \tag{28}$$

Last inner ψ-integration can be performed via polar coordinates as in (15-16)

allowing us to write the Bessel function of the first kind of order 0 as

$$C^{\dagger}Cf(x,y,z) = \frac{2\pi}{z} \int\limits_{\mathbb{R}^2} e^{2\pi i(ux+vy)} \int\limits_{0}^{\pi/2} \widehat{Cf}(u,v,\omega) J_0(2\pi z \tan\omega \sqrt{u^2+v^2})\, \mathrm{d}\omega\, \mathrm{d}u\mathrm{d}v. \tag{29}$$

Last expression differs to inverse formula (21) only by factors $z^3(u^2+v^2)\dfrac{\sin\omega}{\cos^3\omega}$. These factors are seeing as filters that we need to add to data in order to have an exact backprojection inversion procedure.

Therefore, let us define the projections $C^*f(\zeta,\xi,\omega)$ filtered in the Fourier space by the filters

$$\widehat{C^*f}(u,v,\omega) = (u^2+v^2)\frac{\sin\omega}{\cos^3\omega}\widehat{Cf}(u,v,\omega), \tag{30}$$

and lastly we are able to write the inverse formula of the CRT in the form

$$f(x,y,z) = z^3 C^{\dagger}C^* f(x,y,z). \tag{31}$$

5 Simulation results

A numerical object corresponding to a flattened stratigraphic sample is created, reconstructed by means of inversion formula (31) and presented in Figs. 5,6,7 and 8 for different cross sections of a phantom detailed as follows. The phantom is builded with three layers of 512×512 µm^2 regarding its frontal area and about 40 µm of thickness per layer, with electron densities of 0.9, 1.1 and 1.0 respectively. Some grains of random diameter and position are inserted inside the layers, having densities of 1.3 ± 0.1, 6.0 ± 0.5 and 2.0 ± 0.3 for each layer respectively.

5.1 Discretization parameters

The unit length considered in discretizations is 4 µm and thus, each pixel in images represents 16 µm^2.

A square parallel X-ray beam of 256 µm^2 of sectional area crosses a hole in the detector of 144 µm^2 ($\zeta_0 = \xi_0 = 12$ µm). The medium has dimensions of $512 \times 512 \times 128$ µm^3 then we need 32 translations following the $0x$-axis and the same for the Oy-axis, to cover the full medium. The detector plane, located over the xOy-plane at a perpendicular distance of 4 µm to the sample, has an area of 256×256 µm including the hole. Regarding the number of detecting sites, having an area of 1 pixel each, and considering the absence of detecting sites in the hole, we have 4060 detecting sites.

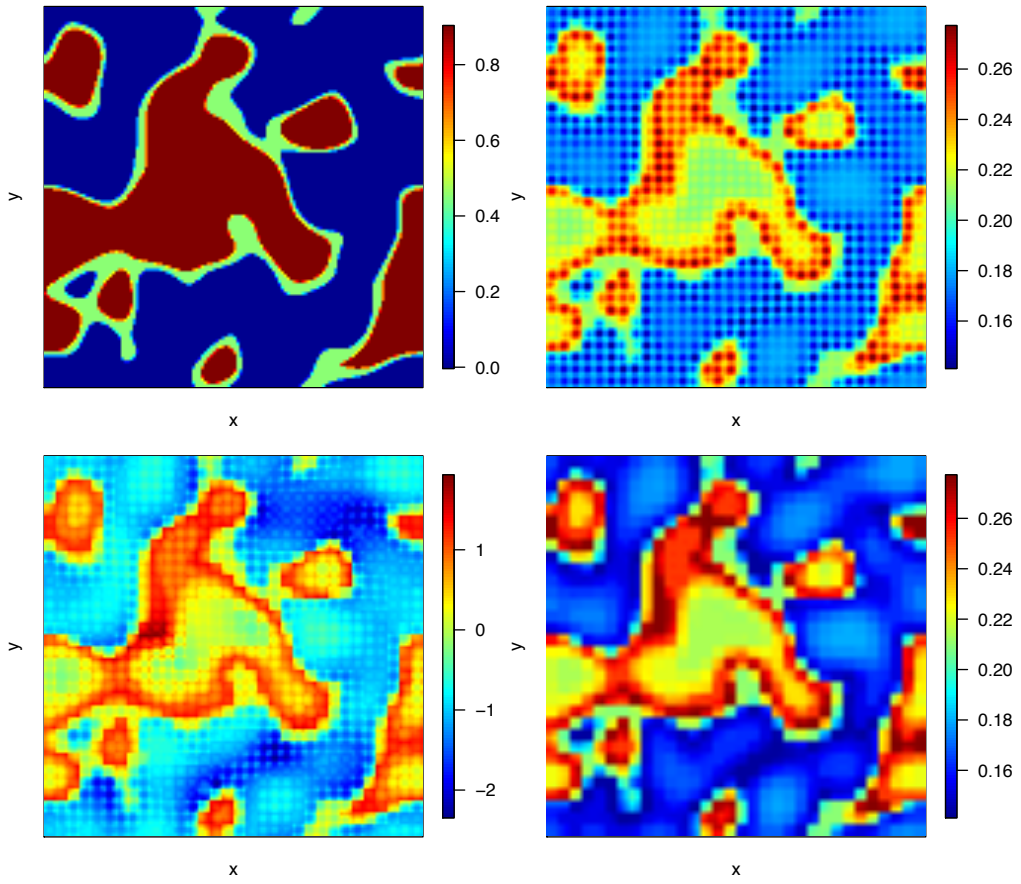

Figure 5: Stratigraphical phantom of dimensions $128 \times 128 \times 32$ voxels. Plane presented: $z = 4$. Top-left: Original phantom, top-right: Direct inversion, bottom-left: Inversion after normalising values following z-axis, bottom-right: Inversion after removing voxels located at edges of single reconstructions of dimensions $4 \times 4 \times 32$ voxels.

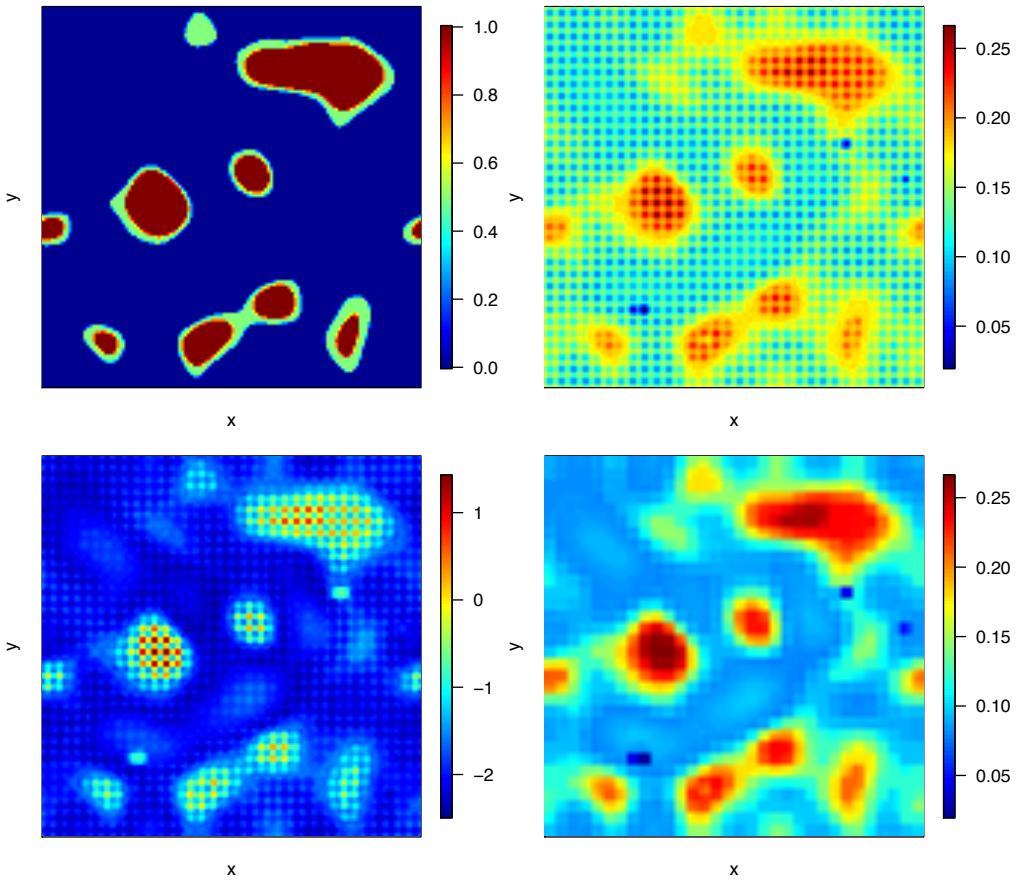

Figure 6: Stratigraphical phantom of dimensions $128 \times 128 \times 32$ voxels. Plane presented: $z = 30$. Same layout as in Fig. 5.

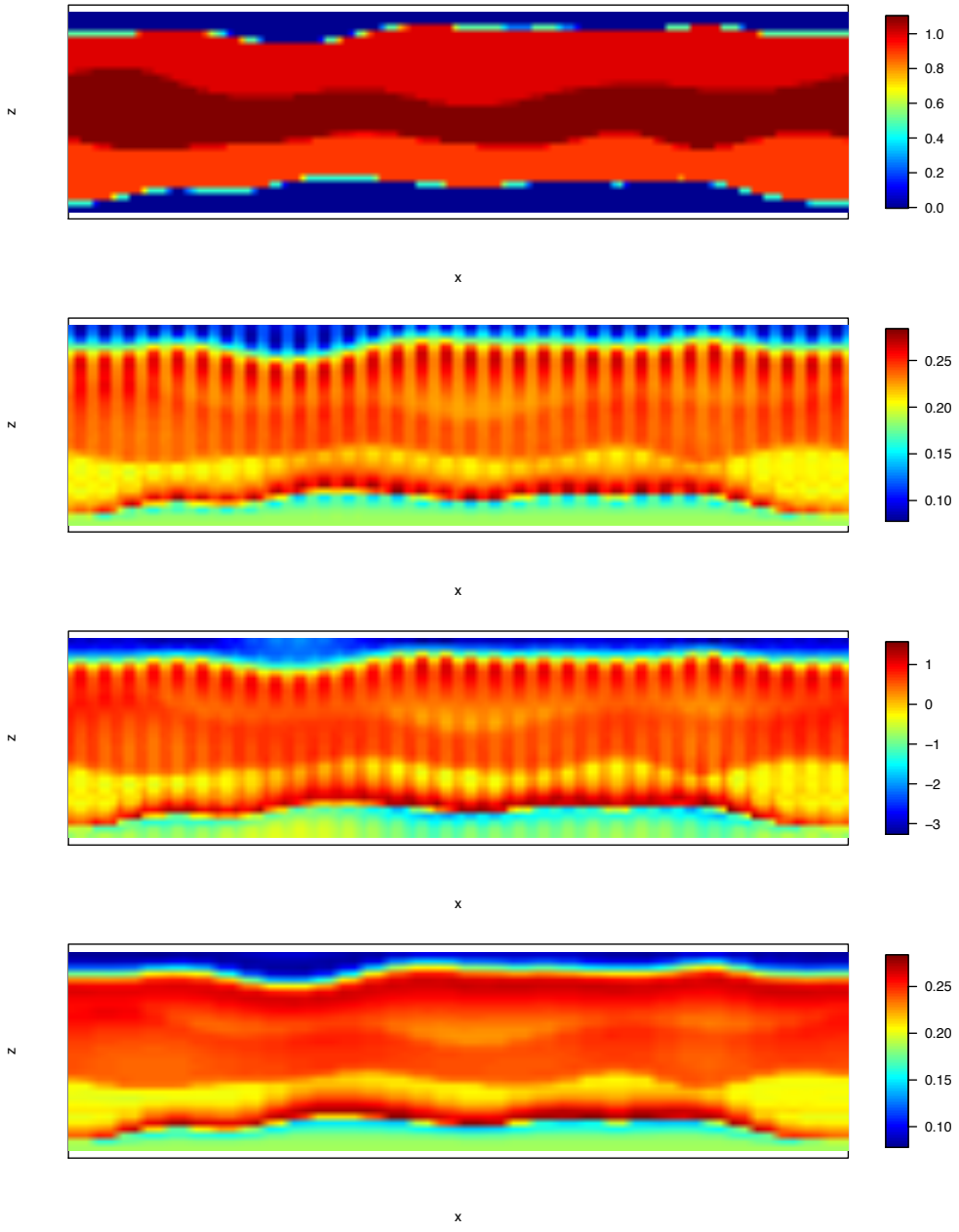

Figure 7: Stratigraphical phantom of dimensions $128 \times 128 \times 32$ voxels. Plane presented: $y = 22$. From top to bottom: Original phantom, direct inversion, inversion after normalising values following z-axis,inversion after removing voxels located at edges of single reconstructions of dimensions $4 \times 4 \times 32$ voxels.

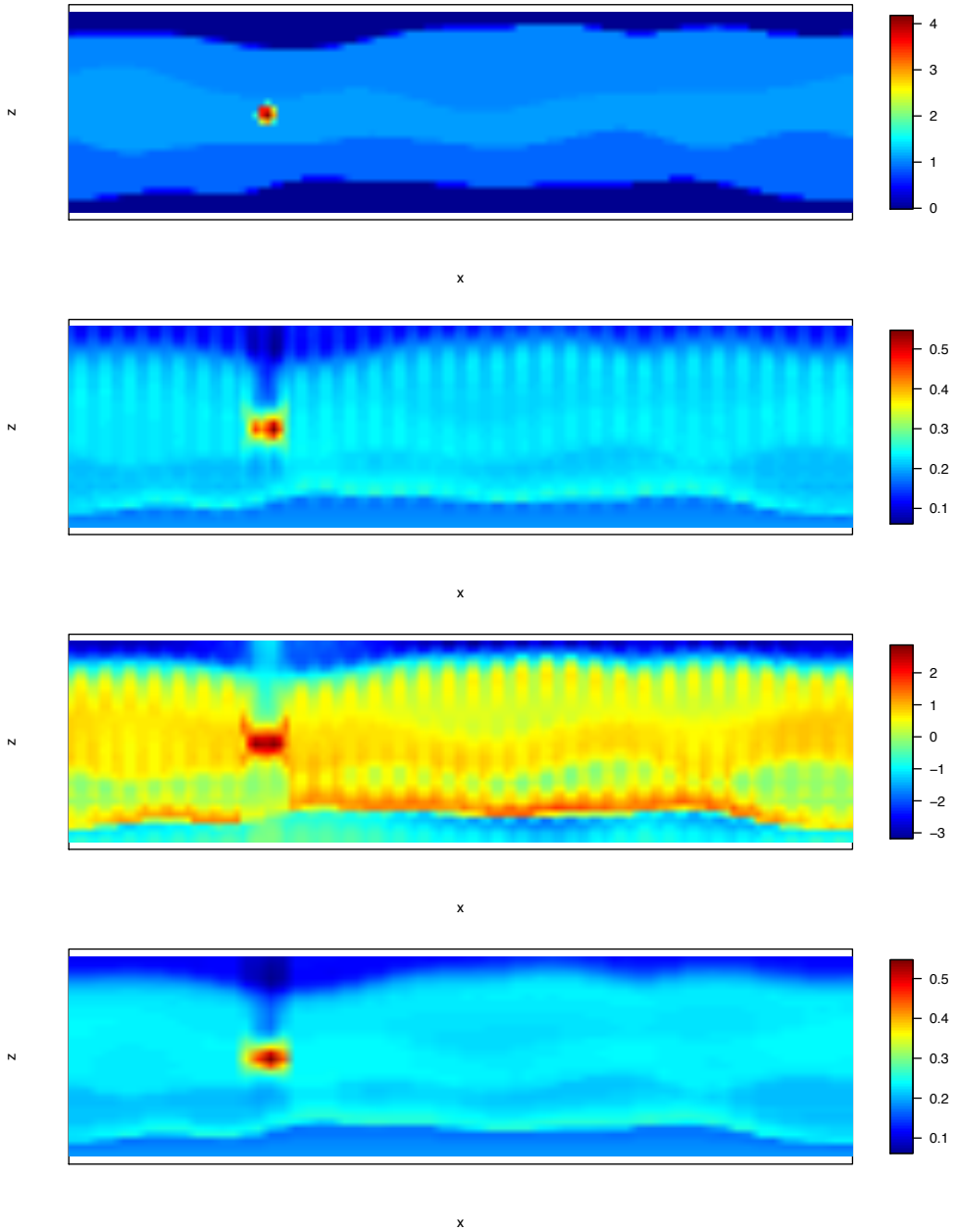

Figure 8: Stratigraphical phantom of dimensions $128 \times 128 \times 32$ voxels. Plane presented: $y = 25$. Same layout as in Fig. 7.

5.2 Numerical image formation

Numerical resolution of integral (3) is performed via the trapezoidal rule with a discretization spatial step $\mathrm{d}r = 4$ µm and an azimuthal angular step $\mathrm{d}\psi = 0.01$ radians. 64 opening angles of the cone from 0 to $\frac{\pi}{2}$ are considered.

5.3 Numerical reconstruction

To compute numerically inversion formula (31) from data $Cf(\zeta, \xi, \omega)$ generated by (3), the procedure works as follows:

1. Filter the projections in the Fourier domain to get $\widehat{C^*f}(\zeta, \xi, \omega)$ appling (30).
2. Perform an inverse Fourier transform to the obtain the filtered projections $C^*f(\zeta, \xi, \omega)$.
3. The backprojection procedure is performed by means of the adjoint transform $C^\dagger$ by (26).
4. Finally, adding the factor z^3, we compute the inversion formula (31).

5.4 Inversion procedure details

Direct application of (31) is first presented in figures, just after the original sample, one can see edge artefacts due to horizontal and vertical translations of the sample and the different scale rates between voxels located at the edge of a single reconstruction and those located at the center. First obvious solution presented is to normalise scales following the z-axis direction, where we can still see this edge artefacts, and conclude that problem is not only about scaling. In the last solution presented, we removed these voxels located at edges, where we can appreciated an encouraging 3D reconstruction of the sample.

A cosine window function was used in the Fourier domain of projections to control high frequencies. Data not recorded in the hole area was filled by a numerical solution of a heat diffusion problem from values of energies captured at the hole edge.

6 Conclusion and perspectives

A X-ray imaging modality based on Compton scattering is presented, the interest is to perform a 3D mapping of flat heritage objects without relaying on relative rotations between object, source and detectors. Both image formation by means of a Conical Radon transform and object reconstruction by a filtered backprojection procedure are exposed and supported with numerical simulations showing feasibility with real data. Results are already very encouraging considering the problem of non-destructive and non-invasive 3D imaging of samples supported by a deep or dense material. Clearly, the current method should still

be worked on to eliminate some artefacts which are strong enough to blur out some of the contrast of the electron density. Yet our methodology enables us to strength our detailed understanding of the image formation process and how it is coupled to the volume reconstruction itself. This is proving instrumental in designing the physical instrument that will ultimately enable such imaging modality.

The current method assumes an exact relationship between the diffusion energy E_ω and the scattering angle ω according to (1). Through Doppler effect and electron binding energy variations this relationship is indeed a non-Dirac probabilistic law. We will use a combination of Monte-Carlo simulations and variational analysis to assess the consequences of our approximation on image formation and volume reconstruction in a current work.

To be able to tackle the system computationally we have first focused on flat objects and using incident energy that optimise the relative importance of single event inelastic scattering versus more complex, multiple scatterings and absorption, interactions. At the chosen incident energy the probability of multiple scattering is very small since the mean free path of the X-ray photons is in the same order of magnitude as the probed volume thickness. When dealing with single scattering and a monochromatic incident beam, it is easy to discriminate photons generated by elastic inelastic scattering events. At the selected incident energy the mean free path attached to scattering is much shorter than that attached to the photoelectric absorption process, in other words the effects of photoelectric absorption is much smaller that scattering effects. It is important to note that inelastically scattered photon have an energy which is in the same domain as the incident photon energy when it comes to relative importance of absorption and scattering.

Still we plan to work on an iterative reconstruction process which, whilst more expensive computationally, will enable us to account also for the smaller effects, photoelectric absorption and multiple scattering, in the produced reconstruction.

Acknowledgment

The authors would like to thank Pierre Gueriau and Mathieu Thoury for their support, discussions and help to acquire images of heritage objects. Annelies van Loon for providing the image of the Rembrandt painting, and the field workers who collected the fossil actinopterygian.

Patricio Guerrero would like to thank the French *Fondation des Sciences du Patrimoine* (PATRIMA LabEx) for providing a PhD grant to support his research work. The same author would also like to thank Javier Cebeiro for his crucial help and discussions.

References

[1] J. Cebeiro, M. Morvidone, and M. K. Nguyen. Back-projection inversion of a conical Radon transform. *Inverse Problems in Sciences and Engineering*, 24(2), Apr. 2015.

[2] P. Gueriau, C. Mocuta, D. B. Dutheil, S. X. Cohen, D. Thiaudire, S. Charbonnier, G. Clmnt, and L. Bertrand. Trace elemental imaging of rare earth elements discriminates tissues at microscale in flat fossils. *Plos One*, 2014.

[3] M. Haltmeier. Exact reconstruction formulas for a radon transform over cones. *Inverse Problems*, 30(3), 2014.

[4] O. Klein and Y. Nishina. The scattering of light by free electrons according to dirac's new relativistic dynamics. *Nature*, 122:398–399, 1928.

[5] M. Morvidone, M. K. Nguyen, T. T. Truong, and H. Zaidi. On the V-line radon transform and its imaging applications. *International Journal of Biomedical Imaging*, 2010.

[6] M. K. Nguyen, T. T. Truong, and P. Grangeat. Radon transforms on a class of cones with fixed axis direction. *Journal of Physics A: Mathematical and General*, 38(37), 2005.

[7] S. J. Norton. Compton scattering tomography. *Journal of Applied Physics*, 76, 1994.

[8] T. T. Truong and M. K. Nguyen. On new V-line radon transforms in $\mathbb{R}^2$ and their inversion. *Journal of Physics A: Mathematical and Theoretical*, 44(7), 2011.

[9] T. T. Truong and M. K. Nguyen. New properties of the V-line radon transform and their imaging applications. *Journal of Physics A: Mathematical and Theoretical*, 48(40), 2015.

Patricio Guerrero, Ph.D. candidate in Computed Tomography, Radon Transforms and applied mathematics since November 2014 at the European research platform on ancient materials IPANEMA under the direction of Serge Cohen, Mai Nguyen and Laurent Dumas. Thesis title: "Compton 2D Imaging for 3D reconstruction".

Mai K. Nguyen received her Ph.D. degree in Signal and Image Processing from Grenoble National Polytechnic Institute, France, in 1988. She is a Professor in the department of Computer Sciences at the University of Cergy-Pontoise since 2005. Her research interests include inverse problems, generalized Radon transforms and their applications in imaging science, scattered ionizing radiation imaging, biomedical imaging, non-destructive evaluation. She is IEEE Senior member.

Laurent Dumas received his Ph.D. degree in applied mathematics from Paris Diderot University 1995. He is currently a professor at Versailles University since 2010. His research interests include numerical analysis, derivative free optimization, uncertainty quantification and have been applied in various engineering and medical fields.

Serge X. Cohen, Ph.D. in Biophysics at EMBL Grenoble. After a postdoctorate period at NKI (Amsterdam) working on shape recognition and statistical learning applied to structural biology he is now a mathematician at CNRS. Since 2010, leading information extraction and analysis scientist at IPANEMA, he focuses on theoretical statistics aspects for spectro-microscopy, and synchrotron radiation tomography for ancient materials.